ACS APPLIED MATERIALS & INTERFACES

Voltage Dependence of Electrolyte Additives for Stabilizing Cathode Electrolyte Interphase

Sven Burke, Renee Wright, Shuang Bai, Lafe Martinson, Nathan Hahn, Kevin Leung, Minghao Zhang,* and Ying Shirley Meng*

Cite This: https://doi.org/10.1021/acsami.5c24930 Read Online

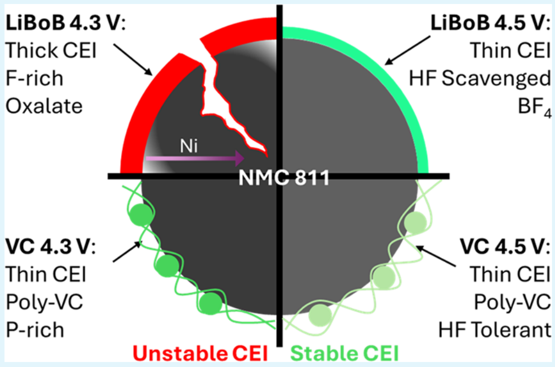

ABSTRACT: Cathode electrolyte interphases (CEIs) formed with the electrolyte additives of vinylene carbonate (VC) and lithium bis(oxalate)-borate (LiBoB) were evaluated after extended cycling up to 4.3 V. At 4.3 V, the Gen2 + LiBoB electrolyte forms a thick fluorine-rich CEI and has poor electrochemical performance (24.4% capacity retention at 460 cycles), while the Gen2 + VC electrolyte forms a thin organic CEI and has superior electrochemical performance (75.0% capacity retention at 1000 cycles). These results demonstrate the superiority of the Gen2 + VC electrolyte-derived CEI at 4.3 V. The poor performance of the Gen2 + LiBoB electrolyte at 4.3 V contradicts the benefits of an HF scavenger above 4.5 V, suggesting voltage-dependent behaviors. To validate the efficacy of the Gen2 + LiBoB electrolyte as an HF scavenger, the higher cycling voltage of 4.5 V was used as a mechanistic probe to evaluate additive efficacy under harsher and HF-rich electrochemical conditions. At 4.5 V, the Gen2 + LiBoB electrolyte demonstrates superior cycling (84.2% capacity retention at 200 cycles) compared to the Gen2 + VC electrolyte (78.5% capacity retention at 200 cycles) and the Gen2 electrolyte system (59.5% capacity retention at 200 cycles).This study demonstrates the voltage-dependent nature of electrolyte additive efficacy and how operating voltage must be a selection criterion for any electrolyte additives to ensure the controlled formation of a robust and high-performance CEI.

KEYWORDS: *batteries, cathodes, interfaces, stability, electrolytes, additives*

INTRODUCTION

Cathode materials are one of the primary limitations on the energy density of contemporary lithium-ion battery technologies, with the cathode accounting for the single largest contribution to the system mass while simultaneously having lower energy density than the associated anode materials.[1−3] To increase the energy density of batteries, there are two approaches: using cathode materials with higher capacity and expanding the operational voltage windows. High-capacity NMC materials with progressively greater nickel content, such as NMC811, can be used; however, these high-capacity cathode materials are often unstable at higher operational voltages beyond 4.3 V.[4−9] Specifically, when operated at elevated voltages, high Ni NMC materials experience significant interfacial and bulk instability, with previous works demonstrating rapid cycling fatigue, structural instability, oxygen loss, and thermal instability.[3−10] While advances in the cathode material itself are required to resolve the bulk instabilities, the stabilization of the interface can be approached through designing the cathode electrolyte reactions. Therefore, understanding the principles that drive cathode electrolyte interphase (CEI) stability and designing electrolytes to ensure stable CEI are crucial for facilitating stable NMC cycling.[11,12]

The CEI is the phase of material that forms on the surface of cathode materials as a result of reactions between the electrolyte species and the cathode material during the cycling of the battery.[1,11−17] The dominant routes for the decomposition of electrolyte species from electrochemical cycling have been demonstrated to be the decomposition of carbonate species, specifically ethylene carbonate (EC), and the protonation of $LiPF_6$ leading to the formation of HF.[18−23] The oxidative byproducts of the carbonate decomposition reactions result in a myriad of oxidized organic compounds that build up on the cathode surfaces. Decomposition reactions can be both chemical and electrochemical. Chemical reactions occur as a function of time and temperature without the need for electrochemical cycling and can even occur between electrode materials and the ambient atmosphere.[24] These chemical reactions will therefore undoubtedly occur to some

Received: December 16, 2025
Revised: April 23, 2026
Accepted: May 21, 2026

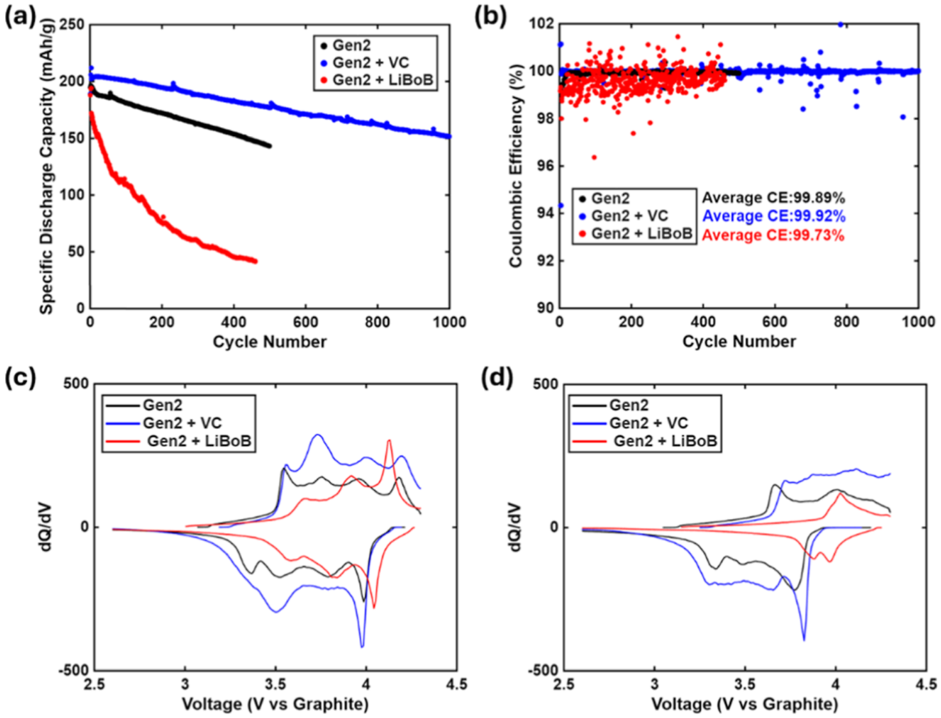

Figure 1. Cycling results from NMC811 full cells with various electrolyte blends cycled to 4.3 V vs graphite: (a) specific discharge capacity over cycling numbers; (b) Coulombic efficiency data for cycling; (c) oxidation and reduction d*Q*/d*V* plots of the first cycle at a rate of C/3; (d) oxidation and reduction d*Q*/d*V* plots of the final cycle, 500th for Gen2, 460th for Gen2 + LiBoB, and 1000th for Gen2 + VC, all at the rate of C/3.

degree upon cathode/electrolyte contact. However, while these reactions might influence the electrochemical behavior, they are not controlled through electrochemistry and therefore are more related to inherent material quality. Electrochemical reactions, by contrast, occur at specific potential(s), or as a result of the induced electrochemical changes to a material, either intended or unintended. These electrochemical reactions, therefore, both influence and are influenced by the history of the cell.[25,26] Therefore, for this investigation, the CEI will refer specifically to the electrochemically derived electrolyte/cathode surface films. During cycling, decomposition reactions cause the buildup of surface products, both organic from solvent breakdown and inorganic from salt and active material breakdown. Uncontrolled surface product buildup can induce cell failure through the loss of electrolyte, degradation of the cathode, and increasing barriers for Li^+ transport.[15,27,28] Significantly, both HF and the decomposition of carbonate species in the electrolyte have been found to accelerate the dissolution of transition metals from NMC cathodes, which in turn accelerates both cathode and anode degradation.[5,29−33] Therefore, an ideal CEI must fill multiple roles, with sufficient coverage and chemical stability to prevent the continual degradation of electrolyte/cathode reactions and HF attack, while simultaneously facilitating effective electrochemical cycling and Li^+ transport.

NMC811 presents additional challenges beyond those posed by the high operational potential. During electrochemical cycling, NMC811 undergoes a number of phase changes driven by the intercalation/deintercalation of lithium from the lattice.[34−36] The volume changes in the NMC811 lattice from these phase changes induce strain in the cathode and the CEI. The cracking in both phases exposes new interfaces for reactions that will drive further electrolyte and cathode decomposition.[35] CEI formation, particularly poor CEI formation, on newly exposed surfaces prevents reversible phase change, leading to crack growth and material degradation. During cycling, NMC also loses oxygen, predominately from the surfaces, leading to the formation of surface phases and rapid oxidation of the electrolyte, accelerating electrolyte decomposition and increasing impedance, respectively.[10,37−40] While the role of the evolved oxygen species in the decomposition of electrolyte and formation of CEI is still debated, this effect over extended cycling can induce failure in NMC cathodes and their CEI.[37−39] The degradation of NMC to form surface phases, such as a rocksalt phase, results in electrochemically inactive surfaces that hinder Li^+ transport, hasten transition-metal dissolution, and induce failure.[10,11,37−40] Therefore, to be compatible with NMC811, the CEI must be stable against the mechanical strains from volume changes during cycling, maintain ionic and electronic conductivities, and withstand oxidative stresses.

This investigation focused on two electrolyte additives, vinylene carbonate (VC) and lithium bis(oxalate)borate (LiBoB), for the baseline electrolyte of 1.2 M $LiPF_6$ in a 3:7 ratio of EC and ethyl methyl carbonate (EMC), known as Gen2 electrolyte. VC was selected as an additive due to the demonstrated efficacy in forming stable SEI.[41,42] Recent investigations also demonstrate that VC can polymerize on cathode surfaces, forming a stable analogue of decomposed electrolyte, leading to passivated surfaces and a stable CEI.[41,43−46] LiBoB serves a different purpose in the electrolyte, with previous studies demonstrating its ability to act as an HF scavenger, effectively suppressing the dissolution of the cathode material through HF attack and preventing further surface degradation.[47,48] LiBoB is also predominantly used at high-voltage conditions (≥4.5 V vs Li/Li^+), where electrolyte degradation and $LiPF_6$ degradation are accelerated, leading to greater HF formation.[48,49] This mechanistic difference allows for the evaluation of each additive's efficacy and comparison of the resultant CEI stabilities with different voltage cutoffs. We thus compare the electrochemical performance of these electrolyte/additive systems in full cells, paired with surface and morphological characterization to inform additive selection criteria. Finally, CEI formation mechanisms are proposed for each additive system, including voltage-dependent performance changes.

■ RESULTS AND DISCUSSION

Results

Electrochemical Performances with a 4.3 V Cutoff. The initial assessment of the electrolyte additive performance on the formation of CEI and stability was conducted in NMC811 | graphite full cells at 4.3 V vs graphite, as shown in Figure 1 (note that for this investigation, all voltages will be provided vs graphite unless otherwise stated). The differences between the electrolyte systems' behavior at 4.3 V are evident based on their capacity retention. The Gen2 system displays capacity retention of 73.4% over 500 cycles. The Gen2 + LiBoB system demonstrates capacity retention of 24.4% after 460 cycles. The Gen2 + VC system demonstrates capacity retention of 87.4% after 500 cycles, and 75.0% after cycling extension to 1,000 cycles, as shown in Figure 1a. Consumption of lithium inventory in each electrolyte system is evident in the initial Coulombic efficiencies of the cells shown in Figure 1b: 80.27%, 86.36%, and 85.16% for the Gen2, Gen2 + LiBoB, and Gen2 + VC systems, respectively. The higher efficiency of the Gen2 + VC and Gen2 + LiBoB systems demonstrates the lower degree of lithium consumption in the initial SEI and CEI reactions compared to the Gen2 system. Continued cycling reveals that the Gen2 + VC system maintains the highest average Coulombic efficiency of the electrolyte blends, representing the lesser degree of parasitic side reactions occurring in the system. The Gen2 + LiBoB system, however, has the lowest average Coulombic efficiency, representing how that system has the greatest degree of parasitic side reactions driving the loss of lithium inventory and cell degradation. These cycling data indicate that while operating at 4.3 V, the VC additive dramatically improves the cycling stability and performance of the full cell, while the LiBoB additive reduces the stability and performance.

The poor performance of the Gen2 + LiBoB electrolyte at 4.3 V is not consistent with the understanding of the additive as an HF scavenger.[47,48] The lower Coulombic efficiency suggests that at 4.3 V, side reactions are encouraged in the Gen2 + LiBoB electrolyte. This becomes particularly apparent in the shift between the dQ/dV redox peaks between the first cycle at C/3 rate and final cycles, where the Gen2 + LiBoB electrolyte system shows more rapid loss of phase transitions than the other electrolytes. The Gen2 + VC and Gen2 + LiBoB systems, however, have additional redox peaks visible in the dQ/dV plot of the first cycle at C/10 rate (Figure S1). An additional oxidation peak near 4.2 V is present for the additive systems, which is not present for the Gen2 system and is not attributable to H_1, M, H_2, or H_3 phase transitions of the NMC.[43] Furthermore, this 4.2 V peak signature is limited to the initial cycle, indicating that the additives undergo electrochemical reactions as soon as the formation cycle. Additionally, the initial oxidation peak voltage is lower in additive systems, further demonstrating that electrolyte additives such as VC and LiBoB alter the CEI formation from initial cycling onward.

Polarization growth in the shift of redox peak potentials from dQ/dV also supports the rapid buildup of surface material for the Gen2 + LiBoB electrolyte system compared to the Gen2 + VC system. The first cycle dQ/dV (Figure S1) shows Gen2 with the greatest initial redox peak to redox peak polarization of 0.21 V, while the Gen2 + VC and the Gen2 + LiBoB samples show lower polarization of 0.12 V. As shown in Figure 1c, the polarization of the cells shifts at a rate of C/3, with the Gen2 cell's polarization decreasing to 0.11 V, while the Gen2 + VC staying constant at 0.12 V and the Gen2 + LiBoB's polarization dropping to 0.05 V. However, by the 100th cycle (Figure S1), the Gen2 + LiBoB system experiences significant polarization increasing to 0.22 V compared to 0.17 V for the Gen2 and 0.18 V for the Gen2 + VC systems. The increase in polarization growth over the course of cycling demonstrates that the CEI for the Gen2 + LiBoB system is continually forming during cycling and is not as stable as the other systems. The resultant unstable CEI could increase polarization through forming more resistive CEI or through damaging the NMC surfaces when cycling. Both scenarios demonstrate that the LiBoB-induced parasitic reactions do not form an ideal CEI.

To help determine the impact of voltage on the electrolyte systems' stability, linear sweep voltammetry (LSV) of all electrolyte systems was performed (Figure S2). The Gen2 + LiBoB system demonstrates the greatest electrochemical stability with no observable increase in current until the potential of 4.5 V, while the Gen2 + VC system has the earliest onsets of decomposition with an increase in current signal as early as 4.2 V. The lower decomposition potential of the Gen2 + VC electrolyte indicates that the formation of the CEI occurred at voltages before bulk electrolyte decomposition. The LSV of the Gen2 + LiBoB system, on the other hand, is more voltage-stable, with current only rising significantly when run at 4.5 V. Reduced current response in the Gen2 + LiBoB electrolyte indicates that a CEI is not formed before bulk solvent degradation, and therefore, the Gen2 + LiBoB electrolyte cannot effectively mitigate this decomposition pathway.

Following the verification of electrolyte voltage stability, electrochemical impedance spectroscopy (EIS) characterized the films formed from electrolyte/electrode reactions. After one formation cycle at C/10, NMC811 full cells showed that in the Gen2 electrolyte, higher voltage cycling increases the overall impedance and film resistance. Film resistance increases relative to charge-transfer resistance, highlighted by R2/R3 ratios, with the R2/R3 of 0.366 (4.3 V) and 0.478 (4.5 V) (Figure S3, Table S1). Half-cell EIS testing shows similar voltage growth trends, with R2/R3 ratios of 0.331 (4.3 V) and 0.374 (4.5 V) (Figure S4, Table S2), confirming that Gen2 forms a passivating CEI (R2/R3 < 1) despite the increased resistance at a higher voltage. Gen2 + VC full cells and half-cells likewise display passivating CEI with R2/R3 values of 0.342 (4.3 V) and 0.378 (4.5 V) for full cells and 0.206 (4.3 V) and 0.207 (4.5 V) for half-cells (Figures S3 and S4, Tables S1 and S2). Consistent R2/R3 ratios for Gen2 + VC samples indicate that VC polymerization occurs before 4.3 V, and CEI growth proceeds regardless of the upper cutoff voltage. Gen2 + LiBoB full cells deviate, with R2/R3 ratios of 5.174 (4.3 V) and 0.580 (4.5 V), demonstrating that low-voltage CEI is nonpassivating and resistive. Although the equivalent circuit

https://doi.org/10.1021/acsami.5c24930
ACS Appl. Mater. Interfaces XXXX, XXX, XXX−XXX

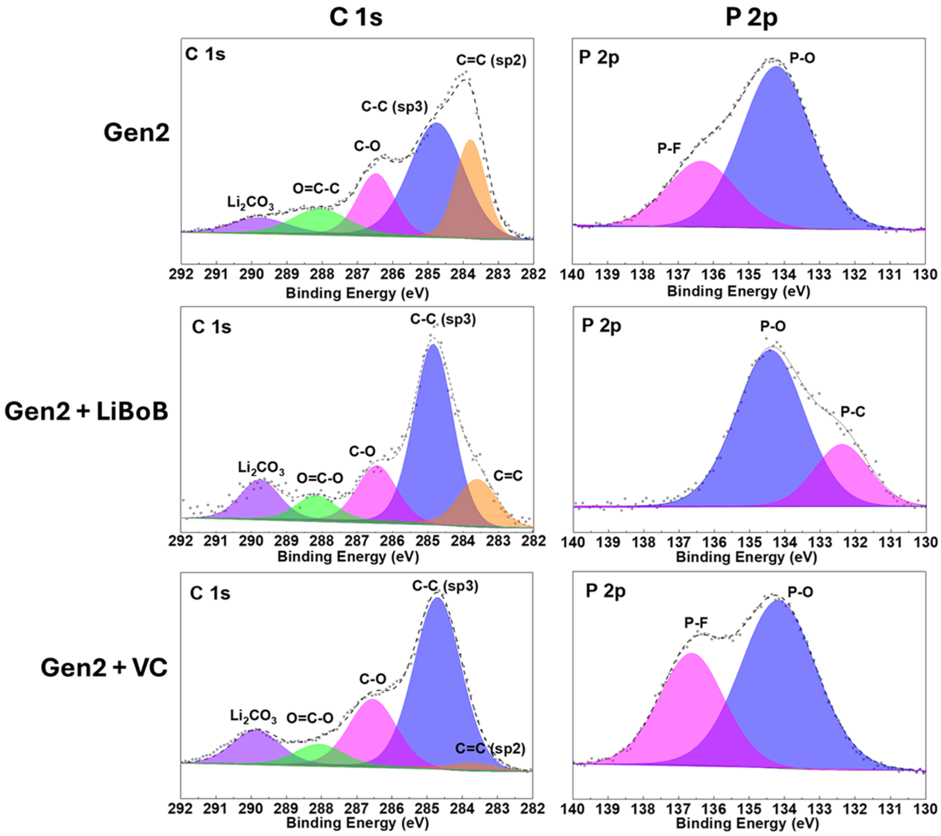

Figure 2. Carbon 1s and phosphorus 2p XPS spectra of the electrodes cycled at 4.3 V in Gen2, Gen2 + LiBoB, and Gen2 + VC electrolytes.

fit for the half-cell data was limited (Figure S5), both film resistance and charge transfer resistance qualitatively appear higher after 4.3 V cycling. EIS data indicate that at higher voltage, Gen2 electrolytes have greater CEI formation, while the VC additive results in consistent voltage-agnostic CEI formation, and the LiBoB additive exhibits voltage-dependent CEI formation.

To determine the impact of the parasitic reactions in the Gen2 + LiBoB electrolyte at 4.3 V, an electrolyte system containing both LiBoB and VC additives was evaluated (Figure S6). The Gen2 + VC + LiBoB electrolyte system has a capacity retention of 77.8% at 500 cycles and an average Coulombic efficiency of 99.88%, suggesting that the combination of VC and LiBoB is not synergistic and provides no mutual benefit. LiBoB, therefore, is not scavenging HF to protect the Gen2 + VC-derived CEI but rather interferes with the formation of stable Gen2 + VC-derived CEI at the moderate conditions of 4.3 V. LSV results indicate that the LiBoB impacts on electrolyte stability are not demonstrated until 4.5 V. If the LiBoB additives were simply ineffective at 4.3 V, the result of mixed VC and LiBoB additive electrolyte should behave more similar to the Gen2 + VC additive, and the Gen2 + LiBoB additive should behave more similar to the Gen2 electrolyte. However, systems with LiBoB operating at 4.3 V consistently underperform, indicating active interference rather than ineffectiveness. The detrimental impact, therefore, is likely the result of the LiBoB additive encouraging parasitic reactions that accelerate the degradation of the system at 4.3 V, demonstrating that additive selection for the formation and stabilization of CEI must consider operational conditions. The ineffective binary electrolyte additive system is not unprecedented, with previous studies indicating that additives can influence each other's solvation structures and decomposition pathways preventing additive cooperation.[13,50,51]

Assessment of CEI Chemistry and Morphology. Chemical information about the mechanistic changes of the electrolyte additives at 4.3 V was provided through X-ray photoelectron spectroscopy (XPS), as shown in Figure 2. The Gen2 system has relatively high sp^2 carbon bonding peaks at 4.3 V with a sp^2/sp^3 carbon ratio of 0.62. The high ratio of sp^2 to sp^3 carbon is consistent with the breakdown of the electrolyte into complex organics.[23] The electrode cycled in the Gen2 + VC electrolyte, by contrast, has a low sp^2 bonding characteristic with an sp^2/sp^3 ratio of 0.07. The reduction in the sp^2 characteristic is consistent with the loss of the C═C bonds of VC during polymerization and the subsequent surface passivation by the Gen2 + VC-derived CEI.[42] The C 1s sp^2/sp^3 ratio shifts in the Gen2 + LiBoB-cycled electrodes to a ratio of 0.20. Compared to Gen2, the lower sp^2/sp^3 ratio of the Gen2 + LiBoB systems indicates less solvent breakdown and a less organic CEI. Formation of a passivating CEI, such as that derived from Gen2 + VC, is demonstrated to reduce electrolyte decomposition and the buildup of complex organics in the CEI.

The C−O to O═C−O bonding of the Gen2 + VC electrolyte system is consistent with the organized ether-rich polymeric VC-derived CEI with high C−O/O═C−O ratios of 2.21 for the C 1s spectra and 0.66 for the O 1s spectra (Figure S7). The Gen2 system's C−O/O═C−O ratios of 1.99 for C 1s and 0.27 for O 1s are consistent with the formation of a mixed organic CEI with a greater carbonate concentration than for the Gen2 + VC case. The CEI from the Gen2 + LiBoB system is highly carbonate-rich, as indicated by the low C−O/O═C−O ratios of 1.62 for C 1s and 0.11 for O 1s,

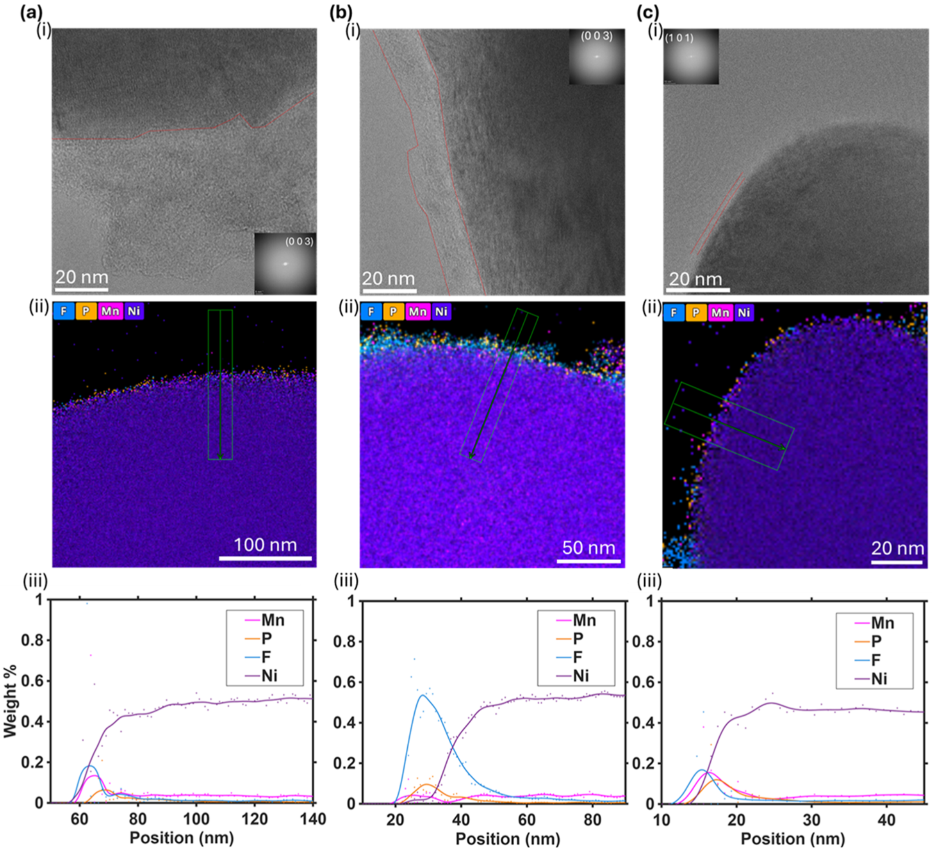

Figure 3. TEM and EDS of cycled NCM811 samples collected at cryogenic temperatures with inert transfer. (a) (i) TEM of NMC811 cycled in Gen2 at 2.6−4.3 V for 500 cycles, (ii) EDS of the large NCM811 particle, (iii) weight fraction of each element along the green arrow in the EDS image. (b) (i) TEM of NMC811 cycled in Gen2 + LiBoB at 2.6−4.3 V for 460 cycles, (ii) EDS of the large NCM811 particle, (iii) weight fraction of each element along the green arrow in the EDS image. (c) (i) TEM of NMC811 cycled in Gen2 + VC at 2.6−4.3 V for 1000 cycles, (ii) EDS of the large NCM811 particle, (iii) weight fraction of each element along the green arrow in the EDS image.

accompanied by an upshift in binding energy consistent with a phosphorus-rich coordination environment. The low carbonate content of the Gen2 + VC electrolyte, therefore, demonstrates that the polymeric Gen2 + VC-derived CEI prevents further carbonate solvent breakdown. The higher carbonate content in the Gen2 and Gen2 + LiBoB systems indicates that the CEI in these systems is the result of greater electrolyte solvent oxidation and breakdown. The data also indicate that the high relative carbonate content in the CEI is detrimental.

The O 1s spectra (Figure S7) provide information about the thickness or the heterogeneity of the CEI. The lattice oxygen signal shown in the O 1s spectra, for both the Gen2 and Gen2 + VC samples, indicates either a thin CEI below the approximately 10 nm XPS penetration depth or a highly heterogeneous CEI. No lattice oxygen signal is observed for the Gen2 + LiBoB system, indicating a CEI thickness exceeding an approximate 10 nm limit. The thicker CEI for the Gen2 + LiBoB system is another indicator of greater electrolyte decomposition as a result of parasitic reactions.

XPS P 2p spectra of the samples demonstrate P−O and P−F bonding in all cycled samples, but the 4.3 V Gen2 + LiBoB sample, and the pristine electrode (Figure S8). The Gen2 electrolyte-cycled electrode has a P−F/P−O ratio of 2.45, indicating that $LiPF_6$ has not experienced a significant degree of P−O-forming hydrolysis reactions. The lower degree of hydrolysis is consistent with low amounts of HF formation, as anticipated at 4.3 V. The Gen2 + VC electrolyte-cycled electrode's P−F/P−O ratio is 1.70, indicating a larger degree of P−O-forming hydrolysis reactions while maintaining high electrochemical performance. Uniquely, the Gen2 + LiBoB electrolyte-cycled electrode does not have any visible P−F, with P−O and P−C bonding present demonstrating a significant degree of $LiPF_6$ breakdown through both hydrolysis for P−O and parasitic routes for P−C. No P−F bonding signal being detected further demonstrates the parasitic shift seen in the Gen2 + LiBoB electrolyte-cycled electrode at 4.3 V. For the F 1s spectra of Gen2 and Gen2 + VC-cycled samples (Figure S7), the organic fluoride signal is higher than that for the Gen2 + LiBoB-cycled sample. The high F^--bonding signal of the Gen2 + LiBoB sample without a strong P−F signal further demonstrates the alteration of the fluorine chemistry of the CEI resulting from the inclusion of the LiBoB additive.

Cumulatively, XPS analysis reveals the voltage dependence of the base chemical environment and the Gen2 electrolyte CEI. The XPS spectra of the Gen2-cycled materials are consistent with greater electrolyte solvent breakdown compared to the hydrolysis of $LiPF_6$ at 4.3 V. For the Gen2 + VC system, XPS indicates the formation of a thin polymeric CEI, mitigating the further decomposition of the electrolyte. However, the Gen2 + LiBoB system's XPS spectra demonstrate parasitic decomposition reactions impacting the C, P, F, and O surface chemistry of the thick CEI.

ICP−MS of post-formation graphite anodes (Tables S10 and S11) revealed elevated concentrations of Li and P in the anodes from Gen2 + LiBoB cycled at 4.3 V, relative to Gen2 and Gen2 + VC samples cycled at 4.3 V. These relatively high

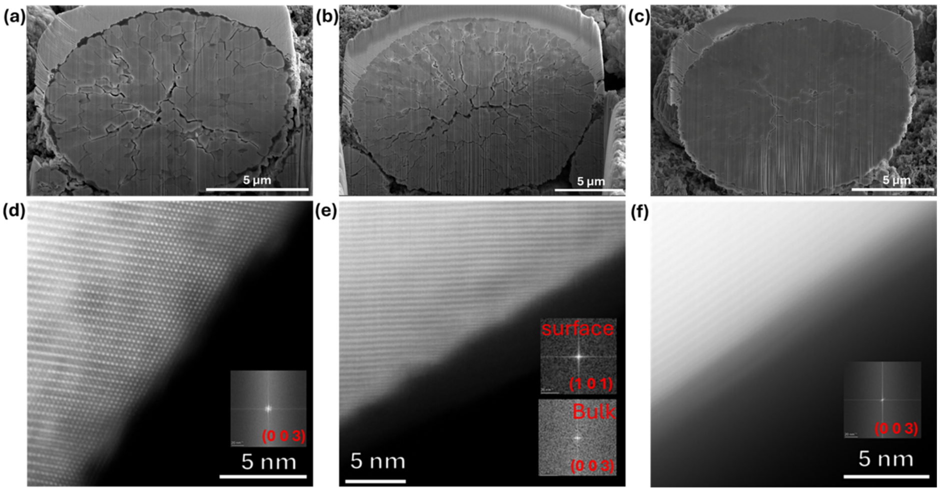

Figure 4. (Top) Postmortem scanning electron microscopy (SEM) images of pFIB cross sections and (Bottom) scanning transmission electron microscopy (STEM) images of NMC811 particles after cycling in electrolyte environments of: (a) Gen2; (b) Gen2 + LiBoB; (c) Gen 2 + VC; (d) Gen2; (e) Gen2 + LiBoB; (f) Gen 2 + VC.

concentrations are consistent with an increased level of electrolyte decomposition during formation cycling. Additionally, the B concentration measured on the 4.3 V Gen2 + LiBoB-cycled anode was greater than that of the 4.5 V Gen2 + LiBoB-cycled anode. Increased B concentration suggests greater LiBoB decomposition at lower voltages, providing more evidence of alternative decomposition pathways for LiBoB at a low voltage. Transition-metal concentrations were observed to be consistently low across all samples, suggesting minimal cathode dissolution during formation cycling.

Energy-dispersive spectroscopy (EDS) of the CEI from cryoTEM (Figure 3) confirms how the various CEI's have different fluorine and phosphorus chemistries. The Gen2 sample has a relatively high concentration of fluorine and phosphorus at the surface of the CEI with an F/P EDS signal ratio of 2.86. The Gen2 + LiBoB sample has a very high fluorine concentration in the CEI with the F/P intensity ratio of 5.58. The Gen2 + VC sample has a lower relative concentration of fluorine with an F/P intensity ratio of 1.41. Relatively high levels of fluorine to phosphorus in the CEI illustrate the decomposition of $LiPF_6$, which has a theoretical F/P ratio of 3.68. A F/P ratio higher than 3.68, such as that with the Gen2 + LiBoB sample, would therefore constitute a phosphorus-poor CEI, with the decomposition of $LiPF_6$ resulting in the buildup of fluorinated species. The accumulation of F^- species in the CEI of the Gen2 + LiBoB sample demonstrates how the inclusion of the LiBoB additive encourages $LiPF_6$ decomposition. Gen2 and Gen2 + VC samples' lower F/P ratios are consistent with the F and P XPS results, and a low F/P ratio demonstrates how $LiPF_6$ decomposition occurs through hydrolysis, reducing F content relative to P content. EDS also elucidated the impact of CEI on the transition metals in the CEI and the transition-metal concentrations near the material surfaces. As shown in Figure 3, all three cycled samples have nickel-poor surfaces before the material bulk is reached. However, the Gen2 + LiBoB sample's surface has the greatest nickel deficiency, indicating a larger degree of transition-metal dissolution than with the other samples.

To directly quantify the CEI thickness for the cycled samples, cryo-TEM with inert transfer was employed for imaging of the primary particle surfaces (Figure 3). Gen2-cycled material has CEI with variable thickness ranging from 20 to 60 nm (±5 nm) where visible. The irregular CEI of the Gen2 sample is consistent with the lattice oxygen observed through XPS and confirms the heterogeneity of the Gen2 CEI. The variability of the Gen2 CEI also indicates that CEI formation without additives is uncontrolled and continuously propagates. CEI derived from the Gen2 + LiBoB electrolyte is 10 ± 2 nm thick. The conformal thick CEI of the Gen2 + LiBoB system is consistent with the previously mentioned increased polarization, and the XPS data in Figure 2 demonstrate no visible lattice oxygen signal. Thick CEI also suggests faster CEI formation from accelerated decomposition reactions or CEI comprised of more insoluble inorganic compounds. Both of these possibilities are supported by data, with XPS and EDS indicating the Gen2 + LiBoB-derived CEI is more fluorine-rich and electrochemistry suggesting rapid decomposition. The Gen2 + VC-derived CEI is 3 ± 2 nm thick. Thin conformal CEI is consistent with the CEI formation through controlled polymerization, and subsequent mitigation of CEI building electrolyte decomposition reactions.

The Gen2-derived CEI has a fluorine and phosphorus ratio that is the closest to that of $LiPF_6$, indicating that at 4.3 V the formation of CEI is predominantly from the breakdown of organic electrolyte solvents rather than from complex $LiPF_6$ decomposition. Thick fluorine-rich CEI and nickel-poor surfaces suggest that the Gen2 + LiBoB electrolyte has more parasitic reactions that drive electrolyte decomposition and transition-metal dissolution, which would accelerate cell failure. The thin conformal and phosphorus-rich CEI of the Gen2 + VC sample suggests that passivation of the NMC surfaces reduces the formation of CEI and accumulation of harmful CEI species.

Postmortem Analysis for CEI Efficacy. Postmortem plasma-focused ion beam (pFIB) cross sections of the cycled NMC811 particles shown in Figure 4 demonstrate the impact of the electrolyte system on the degree of intergranular cracking. The pristine NMC811 particle (Figure S9) has a dense, well-packed structure with no cracking. The Gen2-cycled particle has an extensive degree of cracking, with crack propagation extending throughout the entire particle, and the crack area accounts for 7.42% of the particle's area. The cracks of the Gen2 + LiBoB-cycled sample also propagate through the

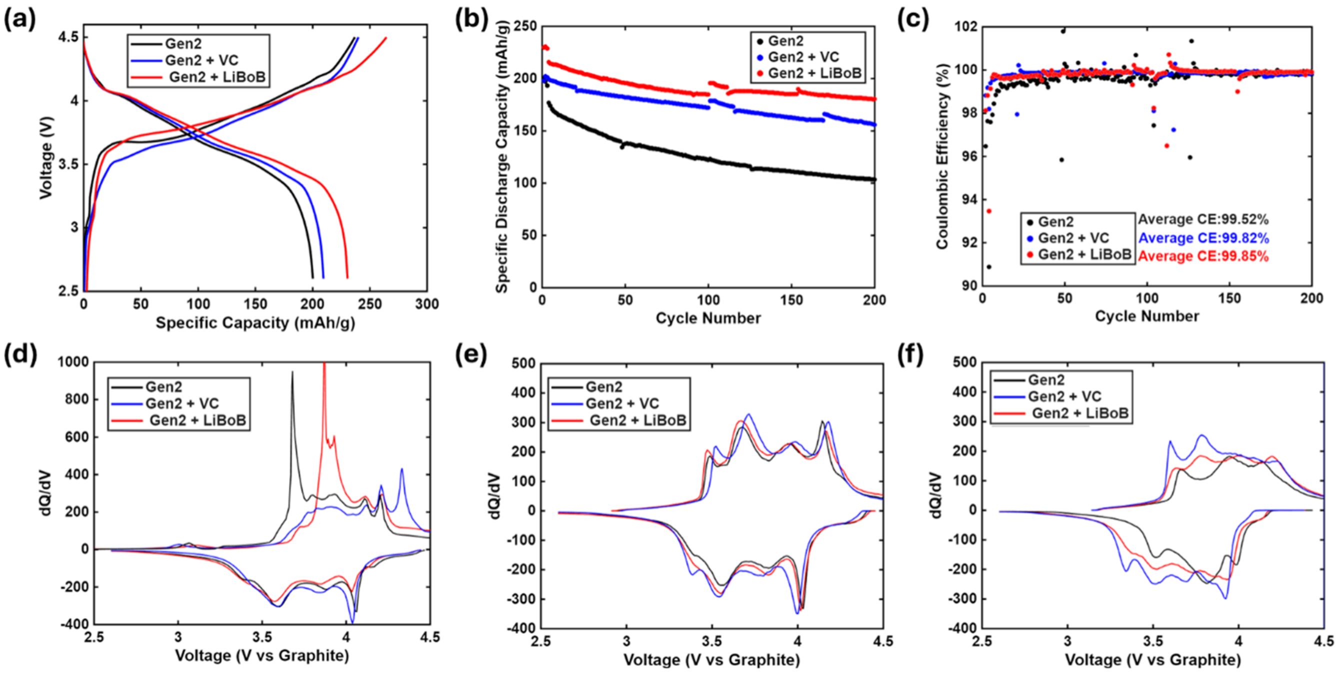

Figure 5. Cycling results from NMC811 full cells with various electrolyte blends and cycled at 4.5 V vs graphite. (a) First cycle C/10 voltage profiles; (b) specific discharge capacity over cycling numbers; (c) Coulombic efficiency data for cycling; (d) oxidation and reduction d*Q*/d*V* plots of the first cycle at a rate of C/10; (e) oxidation and reduction d*Q*/d*V* plots of the first cycle at a rate of C/3; (f) oxidation and reduction dQ/dV plots of the 100th cycle at a rate of C/3.

entire particle. However, they account for a larger 16.01% of the particle area. The Gen2 + VC sample has minor cracks limited to the core of the particle, which account for 2.50% of the particle area. These cracks are not visible on the surfaces of the cycled particles (Figure S10), highlighting the need for cross-section analysis to determine the degree of intergranular cracking. Intergranular cracking is an established failure mechanism of NMC cathode materials, and the observed correlation between the degree of cracking and the overall performance is consistent with this failure mechanism.[35,52]

Intergranular cracking is the result of mechanical stress accumulation at the grain boundaries of the secondary particle from the changes in lattice volume from repeated cycling.[35] Uncontrolled electrolyte reactions with the surfaces of NMC drive degradation of the cathode surfaces, and defect-rich and cracked grain boundaries provide new surfaces for these reactions, leading to continual interfacial reactions that accelerate cell failure. Postmortem STEM data of the cycled NMC surfaces shown in Figure 4 demonstrate clear surface reconstruction for the Gen2 and Gen2 + LiBoB samples when compared to the pristine NMC sample (Figure S11). The reconstructed surfaces are therefore consistent with the observed pFIB cross sections of the cycled Gen2 and Gen2 + LiBoB samples. For the case of the Gen2 + VC electrolyte, the rapid formation of polymeric CEI mitigates degradation reactions at the surfaces and therefore surface reconstruction, as seen through postmortem STEM images in Figure 4. This prevents continuous reactions from new surface exposure from occurring and limits the degree of intergranular cracking (Figure 4). Therefore, more passivating CEIs limit the degree of intergranular cracking.

Electrochemical Evaluation with 4.5 V Cutoff. To elucidate the voltage dependences of the LiBoB and VC electrolyte additives, full cells were evaluated at 4.5 V, as shown in Figure 5. Previous literature has reported LiBoB as an effective HF-scavenging electrolyte additive at voltages higher than 4.5 V.[47,48] At an elevated voltage, the Gen2 system rapidly fails reaching 59.5% capacity retention over 200 cycles, with the initial Coulombic efficiency of 84.51% and average Coulombic efficiency of 99.55%, indicating aggressive decomposition of the electrolyte system, as shown in Figure 5b,c. XPS measurements (Figure S12) confirm accelerated degradation, with greater degrees of fluorinated species and fragmented organics indicating elevated HF levels and greater electrolyte breakdown. With a higher HF content at 4.5 V, the Gen2 + LiBoB system excels, reaching 84.2% capacity retention over 200 cycles and high Coulombic efficiencies of initially 86.83% before averaging to 99.85%. As confirmed through XPS (Figure S12), the electrochemical performance shift is accompanied by a shift in CEI composition, with the P−F/P−O signal ratio indicating robust fluorine management and mitigated electrolyte breakdown. XPS also reveals that at 4.5 V, the Gen2 + LiBoB-derived CEI is thin enough for the observation of the O 1s lattice oxygen peaks, further demonstrating a shift in the Gen2 + LiBoB electrolyte system's behavior from 4.3 to 4.5 V. The Gen2 + VC system outperforms the Gen2 system, reaching 78.5% capacity retention; however, initial Coulombic efficiency is low at 83.46% before averaging out to 99.82% over cycling. As shown in the dQ/dV plots of the first two cycles, the Gen2 + VC system once again has an additional oxidation peak near 4.2 V, likely corresponding to CEI formation, which accounts for its initially lower Coulombic efficiency. Formation of the polymeric Gen2 + VC-derived CEI at 4.5 V is further confirmed by XPS (Figure S12), demonstrating a consistent low C 1s signal of low sp^2 bonding and relatively consistent C−O and O═C−O bonding as well. However, the fluorine signal for the 4.5 V CEI revealed significant buildup of fluorine, suggesting that mitigating electrolyte solvent decomposition is not sufficient for high-performing 4.5 V CEI.

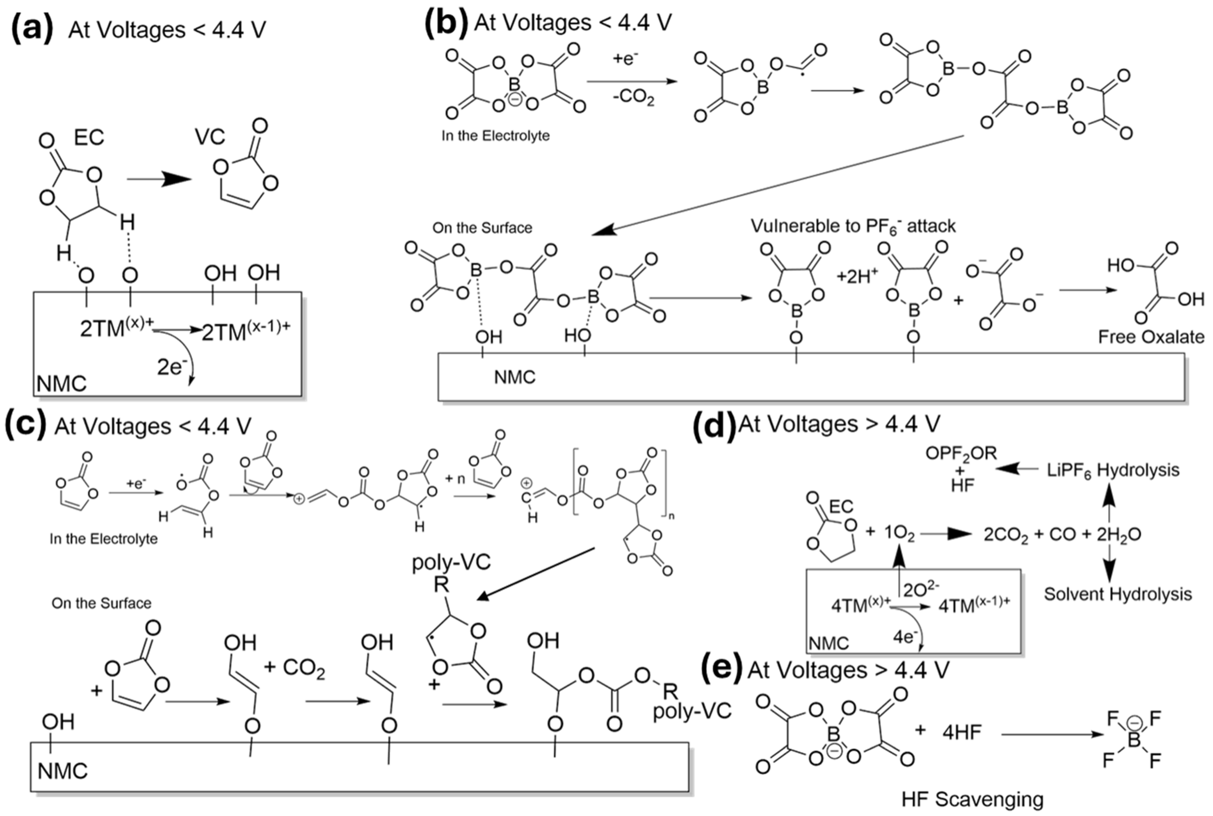

Figure 6. Schematic describing the hypothesized CEI formation mechanism for each electrolyte. (a) Gen 2 without any additives at voltages <4.4 V; (b) Gen 2 + LiBoB at voltages <4.4 V; (c) Gen2 + VC at voltages <4.4 V; (d) Gen 2 without any additives at voltages >4.4 V; (e) Gen 2 + LiBoB at voltages >4.4 V. For this figure, voltages are measured with reference to Li/Li^+.[43,46−49]

Cycling at 4.5 V introduces accelerated electrolyte breakdown and an increased HF concentration. As demonstrated by the shift in the dQ/dV curves between the first and 100th cycles, broadening of peaks indicates the accelerated structural degradation of NMC811 at 4.5 V compared to that at 4.3 V. Loss of peak intensity and redox peak broadening in the dQ/dV curves indicate the loss of discrete phase transitions during cycling. Significantly, both Gen2 + LiBoB and Gen2 + VC systems have greater intensity and peak retention than those of the Gen2 system, indicating less structural degradation. Additionally, dQ/dV analysis elucidates that the degrees of polarization growth for the Gen2 + LiBoB and Gen2 + VC systems are similar, with 0.21 V of growth over the first 100 cycles. The comparable polarization growth between the two systems suggests a comparable CEI growth between the two systems. By probing the impact of 4.5 V cycling on the two electrolyte systems, it becomes clear that at 4.5 V, the LiBoB additive is indeed an effective HF scavenger, mitigating system degradation and allowing for the formation of an effective CEI.

■ DISCUSSION

This investigation demonstrates that no singular voltage threshold provides an accurate assessment of electrolyte additives' efficacy. While the moderate cycling voltages of 4.3 V provide an environment where stable CEI is essential for high performance, it might not be sufficient to determine how additives are impacted by high HF concentrations formed at higher voltages. As compared in Figure 1 and Figure 5, the VC additive is highly effective at 4.3 V, and it is eclipsed by the LiBoB additive at 4.5 V.

Through investigating the composition of CEI derived from these electrolyte blends and their impact on cell failure, it is clear that an effective electrolyte needs to encourage controlled and limited CEI growth. Figures 2 and 3 demonstrate that Gen2 electrolyte cycling at 4.3 V leads to continuous electrolyte breakdown and the formation of heterogeneous CEI. The composition of the Gen2-derived CEI is also demonstrated to be predominantly complex fragmented organics, indicating that at 4.3 V the primary electrolytel NMC degradation reactions are solvent decomposition reactions, as shown in Figure 6a. The uncontrolled solvent decomposition drives degradation of the NMC and causes the formation of inconsistent and nonpassivating CEI. The degradation of the NMC surfaces drives NMC surface reconstruction and passivation, leading to an accumulation of stress and the formation of intergranular cracks that lead to failure, as shown in Figure 4. When the voltage of this system is increased to 4.5 V, the degradation mechanism shifts, as seen in Figure 6d. The greater HF content at an elevated voltage introduces an additional decomposition route besides solvent breakdown, which accelerates failure and changes the characteristics of the CEI to a more fluorine-rich environment.

The VC electrolyte additive is highly effective at mitigating electrolyte breakdown at 4.3 V, and the Gen2 + VC electrolyte forms a highly effective CEI that passivates the NMC surface. Polymerization of the VC additive occurs at relatively low voltages and forms a robust CEI during formation cycling, preventing the continuous breakdown of electrolyte solvents, as shown in Figure 6c. During this passivating polymerization, VC is consumed to form the CEI, and the reaction terminates either when the VC monomer supply is fully exhausted or if the CEI passivates the surface enough to prevent electron transfer. Both of these routes limit and control the growth of the CEI. Cycling at 4.5 V reduces the efficacy of the Gen2 + VC systems, as shown in Figure 5. Cycling at 4.5 V does not impact VC polymerization and surface passivation for NMC, indicating that solvent decomposition is still mitigated. However, at 4.5 V, greater HF concentration and NMC instability introduce degradation routes that the Gen2 + VC electrolyte does not address as effectively. This is particularly observed through the accumulation of fluorinated species in the Gen2 + VC-derived CEI at 4.5 V. The VC additive is therefore highly effective at preventing the electrolyte solvent decomposition, but at elevated voltages where multiple decomposition pathways are present, the VC additive's efficacy is reduced.

The LiBoB additive is an excellent example of how the shift in electrochemical environment impacts additive efficacy. At 4.3 V, the data demonstrate the LiBoB additive accelerates cell failure as the Gen2 + LiBoB electrolyte forms a thick inorganic and ineffective CEI through the parasitic decomposition of the electrolyte. Observation of increased O═C−O bonding signal and the observed loss of transition-metal EDS signal after cycling at 4.3 V suggest the parasitic decomposition of the Gen2 + LiBoB electrolyte results in free oxalate species that drive transition-metal loss and NMC degradation, as outlined in Figure 6b. While oxalates are effective chelating agents that can help explain the loss of transition metals at a moderate voltage, direct spectroscopic studies for the confirmation of the 4.3 V oxalate mechanism are encouraged.[53] Critically, at 4.3 V, the Gen2 + LiBoB system provides no moderation or limitation on solvent decomposition, with the loss of transition metals and degradation of NMC exposing new reactive surfaces and encouraging breakdown. Alternative fluorine decomposition and increased fluorine ion concentration in the Gen2 + LiBoB-derived CEI further demonstrates that at lower voltage, LiBoB encourages $LiPF_6$ decomposition. Boron has a high affinity for F^-, making LiBoB an effective HF scavenger, but in environments with reduced HF concentration, $LIPF_6$ would be the predominant source of F^-, and LiBoB will interact with $LiPF_6$.[54] For this case, LiBoB/$LiPF_6$ interactions weaken the P−F bonding, promoting F reactivity, resulting in increased parasitic reactions. This mechanism suggests that at low voltages the concentration of LiBoB can be externally limited and be decreased to mitigate the degree of harmful parasitic interactions, but more work is needed to determine this complex relationship at low voltages. However, at 4.5 V, the Gen2 + LiBoB system's reactions are more controlled and limited. As seen in Figure 6e, when LiBoB scavenges HF, it is consumed to form BF_4, limiting the scope of the LiBoB reactions to the consumption of LiBoB itself. This means that similar to the Gen2 + VC system, the Gen2 + LiBoB system at 4.5 V undergoes controlled and limited reactions, with HF regulating the LiBoB additive in much the same way LiBoB regulates HF. Therefore, through scavenging HF, the LiBoB additive simultaneously prevents HF-induced cell degradation and protects the CEI during formation. In turn, by converting LiBoB to BF_4, the uncontrolled degradation reactions that damage the CEI are also prevented. These findings demonstrate that as an electrolyte additive, LiBoB is best suited to high stress cycling conditions with high HF concentrations that require scavenging.

These insights from the Gen2 + VC and Gen2 + LiBoB electrolyte systems provide clear design criteria for forming stable CEI. The primary insight is that regardless of the cycling conditions, the formation of a CEI should be through inherently self-limiting reactions. This property will provide greater control of the overall electrolyte decomposition and result in a conformal CEI. For controlled CEI formation, the additive concentration will need to be investigated to ensure that the resultant CEI is optimized for passivation without increasing interfacial resistance and interparticle stress. The VC and LiBoB additives have different mechanisms for the regulation of their CEI formation and control of electrolyte decomposition. However, both high-performing systems, the Gen2 + VC system at 4.3 V and the Gen2 + LiBoB system at 4.5 V, result in thin CEI, demonstrating the efficacy of limited and controlled CEI growth.

The mechanistic test at 4.5 V demonstrates that the more aggressive cycling conditions require additives to specifically address the additional degradation mechanisms. However, as demonstrated with LiBoB, these additives should only be considered for environments where the degradation mechanism(s) they target are dominant, such as HF scavenging. Otherwise, the additives can easily become contaminants and cause unfavorable parasitic reactions. More generally, for moderate voltage conditions, such as 4.3 V, where electrolyte decomposition is the primary concern, controlled sacrificial CEI-forming additives should be used. Mechanism-specific additives should only be used at voltages where their targeted degradation pathway dominates, such as HF regulation at ≥4.5 V.

Additionally, our data suggest that effective additives should result in thin, conformal CEI as opposed to thick or heterogeneous CEI. The formation of a thin CEI generally indicates controlled electrolyte decomposition and fewer interfacial barriers. The thick CEI suggests more rapid CEI formation and, by extension, rapid degradation reactions. However, while generally thicker CEI presents larger interfacial barriers, the thickness of the CEI is only a reliable proxy for CEI resistance across samples of the same chemistry, as demonstrated through EIS measurement of film resistance. At 4.3 V, these principles are effectively demonstrated by the thin and effective CEI derived from the Gen2 + VC electrolyte compared with the thick ineffective CEI derived from the Gen2 + LiBoB electrolyte.

■ CONCLUSIONS

This study demonstrates how voltage can impact the CEI formed from electrolytes containing VC and LiBoB additives. The VC additive excels at 4.3 V, forming an early-stage CEI that prevents the degradation of other carbonate species from the electrolyte. The Gen2 + LiBoB electrolyte at 4.3 V has poor performance, promoting the formation of a thick, ineffective CEI composed of organophosphates and other parasitic byproducts. At 4.5 V, the HF concentration in the electrochemical environment increases, and the efficacy of the electrolyte + additive systems changes. Gen2 + LiBoB is the most effective electrolyte in the HF-rich 4.5 V environment, and in this environment, HF scavenging is essential for CEI preservation and performance. Gen2 + VC at 4.5 V still mitigates the decomposition of electrolyte solvents, and the Gen2 system is outperformed. However, the accumulation of fluorine prevents the Gen2 + VC electrolyte from exceeding the performance of the Gen2 + LiBoB electrolyte, highlighting how each additive addresses different degradation mechanisms. These results establish three design principles for electrolyte

https://doi.org/10.1021/acsami.5c24930

additives and the formation of stable CEI: (1) an additive must specifically target a degradation mechanism that occurs at that operational voltage; (2) electrolyte additives should have self-regulating reactions that serve to mitigate or prevent continuous reactions; and (3) electrolyte additives should promote the quick and early formation of thin CEI. Through these design principles, this study provides a framework for the selection of CEI-stabilizing electrolyte additives for moderate to elevated voltages.

■ EXPERIMENTAL/METHODS

Electrode Fabrication

Electrodes were prepared by mixing the prepared cathode materials with polyvinylidene fluoride (PVDF), C45 carbon black, and *N*-methyl-2-pyrrolidone (NMP) in a 96:2:2 mass ratio. PVDF was first solvated in NMP before the introduction of carbon additives, and finally, the NMC811 active material was added to preserve morphology. The NMC811 material was provided by Targray Materials through Pacific Northwest National Lab. All mixing was conducted through planetary mixing with a Thinky brand mill. The final slurry was coated onto a 20 μm aluminum foil with a doctor blade using an MTI-auto blade coater machine to reach an even deposition of slurry. This slurry was then dried in a 100 °C oven in air for 12 h before being transferred to a 100 °C vacuum oven for 12 h. Electrodes were then calendared to reach a target porosity of 30–35%. All electrodes were stored in a 70 °C vacuum oven to prevent exposure to moisture.

Coin Cell Assembly

Coin cells were prepared by punching 14 mm disks of the desired electrodes. These electrodes were then assembled into 2032 coin cells using Hosen 316 stainless steel components, Celgard 2320 separator, and 15 mm punched graphite electrodes provided by the CAMP facility at Argonne National Laboratory. The N/P ratio of each cell was balanced to be 1.10 ± 0.05 for full-cell assembly. The electrolyte was used at the 50 μL level with the base electrolyte of 1.2 M $LiPF_6$ EC: EMC 3:7, known as Gen2. Variations of Gen2 electrolytes with the additives were used at the same volume. Coin cells were crimped using a Honsen automatic coin cell crimping machine.

Electrolyte Preparation

Stock 1.2 M $LiPF_6$ EC: EMC 3:7 solution was obtained from Tomiyama Pure Chemical Industries and stored in a Teflon-lined aluminum container in an Ar gas-filled glovebox. This stock solution was used as is for any sample cycled in Gen2. For the preparation of electrolyte blends, VC was obtained from the distillation of VC stock solution obtained from Sigma-Aldrich; this distilled solution was then added to the Gen2 stock solution at 2 wt % and stored in a sealed container in a refrigerator in an Ar gas-filled glovebox. The lithium bis(oxalate)borate was purchased from Sigma-Aldrich and stored in a refrigerator in an Ar gas-filled glovebox. Preparation of the LiBoB and Gen2 solution was done through adding 2 wt % of the LiBoB solid to the Gen2 electrolyte and mixing for 10 min before storing in the refrigerator for 1 h, before stirring again for 10 min. This process was repeated until 2 stirs had been done without seeing any LiBoB solids remaining in solutions (3–4 times), at which point the solution was stored in a sealed container in a refrigerator of an Ar-filled glovebox. The refrigerator temperature was set to 0 °C for all storage.

Electrochemical Testing

Full-cell testing was conducted on a Maccor potentiostat at 30 °C, with an initial formation cycling of three cycles at a C/10 rate, before the remaining cycling was conducted at a rate of C/3. Cycling occurred at voltages of 2.6–4.3 V vs graphite or at 2.6–4.5 V vs graphite as specified. EIS testing was carried out on a Biologic brand potentiostat/glavanostat on pEIS mode between 10 mHz and 100 kHz with a voltage amplitude of 5 mV, carried out after one cycle at a rate of C/10 between the voltages of 2.6–4.3 V or at 2.6–4.5 V vs lithium or graphite as specified. Measurement was conducted at ambient temperature (25 °C). Equivalent circuit model fitting was conducted on the zFit software and weighted by $\chi^2/|Z|^2$, with the circuit model being visible in Figure S5.

FIB-SEM Measurements

FIB-SEM measurements were conducted on a Thermo Fisher Scientific Helios Hydra Plasma FIB. Prior to cross-sectioning, a protective 2 μm tungsten layer was deposited on the secondary particles. FIB cross-sectioning was then conducted with Xe plasma at an acceleration voltage of 30 kV and a current of 1.5 nA, before polishing was conducted at 30 kV and 0.3 nA of current. After sectioning, the SEM instrument was used in secondary electron imaging mode with a current of 0.1 nA and an acceleration voltage of 5 kV. Work was performed at the CNM at Argonne National Laboratory, proposal number 83419.

STEM Measurements

STEM measurements of NMC particles were conducted on a Thermo Fisher Scientific Spectra200 system, using a double-tilt holder with acceleration voltages of 200 kV. All experiments with the STEM system were conducted at ambient temperature. Work was performed at the CNM at Argonne National Laboratory, proposal no. 83419.

Cryo-TEM and EDS Measurements

Cryo-TEM and EDS measurements of NMC particles were conducted on a Thermo Fisher Scientific Spectra 300 Ultra X/Illiad analytical electron microscope at Argonne National Laboratory. High-resolution TEM phase contrast images were collected at 300 kV on the Thermo Fisher Scientific Falcon 4i camera under a dose rate of ∼100 e/A2/s at 4K2 pixel resolution with an exposure time of 0.991 s per frame. The chemical spectra and images were acquired on an UltraX detector. The samples were securely transferred using a Simple Origin inert gas transfer holder from the glovebox to the TEM column to avoid any exposure to air or moisture.

XPS Measurements

XPS measurements of 4.3 V-cycled cathodes were taken on a Kratos AXIS Supra system operated at a base pressure better than 5×10^{-9} Torr, using a monochromatic Al Kα X-ray source (λ = 1486.6 eV). Surveys and high-resolution spectra for elements of interest were taken on each sample. Spectra were obtained using a large analyzer spot size and a pass energy of 160 eV for all surveys and 20 eV for the high-resolution spectra. Charge compensation was done using a charge neutralizer with a filament current of 0.42 A. XPS measurements at 4.5 V were taken on a Thermo Fisher Scientific ESCALAB 250 Xi system available at Northwestern University's NUANCE facility. The machine was operated at a base pressure better than 5×10^{-9} Torr, using a monochromatic Al Kα X-ray source (λ = 1486.6 eV), with survey and other scanning conditions consistent with the previous 4.3 V measurements. The processing of XPS was conducted through the use of the CasaXPS software, which was exported before finalized plots in OriginPro.

ICP–MS Measurements

ICP–MS analysis was performed on a Thermo iCAP Q ICP–MS or Thermo iCAP RQ ICP–MS instrument on samples that were prepared following the procedure below. NMC811|graphite full cells were made with the electrolyte blends described and then cycled three times at a rate of C/10 with the specified upper cutoff voltages. After these formation cycles, the cells were disassembled, and graphite was removed and washed with 100 μL of trace metal basis DMC, before drying. The wash solution from each anode was collected and diluted at 100× with 3% HNO_3 ICP–MS standard solution before ICP–MS analysis was conducted. After drying, graphite was scraped off the anodes and allowed to dissolve in Aqua-Rega for 3 days before dilution by 10× with 3% HNO_3 ICP–MS standard solution. ICP of Li, B, and P was conducted in standard collection mode, with Ni, Co, and Mn collected in kinetic energy discrimination mode. All coin cell disassembly, washing, and drying were conducted in a dry argon environment.

■ ASSOCIATED CONTENT

Supporting Information

The Supporting Information is available free of charge at https://pubs.acs.org/doi/10.1021/acsami.5c24930.

> Additional cycling data; additional electrochemical tests like LSV or EIS of the electrolyte blends and cathodes; additional XPS spectra pre- and postcycling; additional microscopy images of materials pre- and postcycling including STEM and FIB/SEM; data related to the; and results from ICP of anodes cycled in electrodes (PDF)

■ AUTHOR INFORMATION

Corresponding Authors

Minghao Zhang − *Pritzker School of Molecular Engineering, University of Chicago, Chicago, Illinois 60637, United States; Electrochemical Energy Storage Department, Chemical Science and Engineering Division, Argonne National Laboratory, Lemont, Illinois 60439, United States;* Email: miz016@uchicago.edu

Ying Shirley Meng − *Pritzker School of Molecular Engineering, University of Chicago, Chicago, Illinois 60637, United States; Electrochemical Energy Storage Department, Chemical Science and Engineering Division, Argonne National Laboratory, Lemont, Illinois 60439, United States;* orcid.org/0000-0001-8936-8845; Email: shirleymeng@uchicago.edu

Authors

Sven Burke − *Pritzker School of Molecular Engineering, University of Chicago, Chicago, Illinois 60637, United States; Electrochemical Energy Storage Department, Chemical Science and Engineering Division, Argonne National Laboratory, Lemont, Illinois 60439, United States*

Renee Wright − *Pritzker School of Molecular Engineering, University of Chicago, Chicago, Illinois 60637, United States*

Shuang Bai − *Electrochemical Energy Storage Department, Chemical Science and Engineering Division, Argonne National Laboratory, Lemont, Illinois 60439, United States*

Lafe Martinson − *Pritzker School of Molecular Engineering, University of Chicago, Chicago, Illinois 60637, United States*

Nathan Hahn − *Material, Physical and Chemical Sciences Center, Sandia National Laboratories, Albuquerque, New Mexico 87123, United States;* orcid.org/0000-0001-6187-4068

Kevin Leung − *Biological, Earth Systems, Radiation, and Signature Science, Technology, & Engineering Center, Sandia National Laboratories, Albuquerque, New Mexico 87123, United States;* orcid.org/0000-0003-1397-3752

Complete contact information is available at: https://pubs.acs.org/10.1021/acsami.5c24930

Notes

The authors declare no competing financial interest.

■ ACKNOWLEDGMENTS

XPS of 4.5 V-cycled electrodes made use of the NUFAB facility (RRID:SCR_017779) of Northwestern University's NUANCE Center, which has received support from the IIN and Northwestern's MRSEC program (NSF DMR-2308691). TEM, STEM, SEM, and FIB work performed at the Center for Nanoscale Materials, a U.S. Department of Energy Office of Science User Facility, was supported by the U.S. DOE, Office of Basic Energy Sciences, under Contract No. DE-AC02-06CH11357. This article has been authored by an employee of National Technology & Engineering Solutions of Sandia, LLC under Contract No. DE-NA0003525 with the U.S. Department of Energy (DOE). The employee owns all right, title and interest in and to the article and is solely responsible for its contents. The United States Government retains and the publisher, by accepting the article for publication, acknowledges that the United States Government retains a nonexclusive, paid-up, irrevocable, worldwide license to publish or reproduce the published form of this article or allow others to do so, for United States Government purposes. The DOE will provide public access to these results of federally sponsored research in accordance with the DOE Public Access Plan https://www.energy.gov/downloads/doe-public-access-plan. This paper describes objective technical results and analysis. Any subjective views or opinions that might be expressed in the paper do not necessarily represent the views of the U.S. Department of Energy or the United States Government. This work was supported by the Assistant Secretary for Energy Efficiency and Renewable Energy, Office of Vehicle Technologies of the U.S. Department of Energy (DOE) through Cathode-Electrolyte Interphase (CEI) Consortium.

■ REFERENCES

(1) Goodenough, J. B.; Park, K.-S. The Li-Ion Rechargeable Battery: A Perspective. *J. Am. Chem. Soc.* **2013**, *135*, 1167−1176.

(2) Li, M.; Lu, J.; Chen, Z.; Amine, K. 30 Years of Lithium-Ion Batteries. *Adv. Mater.* **2018**, *30*, 1800561.

(3) Grey, C. P.; Hall, D. S. Prospects for lithium-ion batteries and beyond—a 2030 vision. *Nat. Commun.* **2020**, *11*, 6279.

(4) Kim, J.; Lee, H.; Cha, H.; Yoon, M.; Park, M.; Cho, J. Prospect and Reality of Ni-Rich Cathode for Commercialization. *Adv. Energy Mater.* **2018**, *8*, 1702028.

(5) Dose, W. M.; et al. Onset Potential for Electrolyte Oxidation and Ni-Rich Cathode Degradation in Lithium-Ion Batteries. *ACS Energy Lett.* **2022**, *7*, 3524−3530.

(6) Streich, D.; et al. Operando Monitoring of Early Ni-mediated Surface Reconstruction in Layered Lithiated Ni−Co−Mn Oxides | The Journal of Physical Chemistry C. *J. Phys. Chem. C* **2017**, *121*, 13481.

(7) Märker, K.; Reeves, P. J.; Xu, C.; Griffith, K. J.; Grey, C. P. Evolution of Structure and Lithium Dynamics in LiNi0.8Mn0.1-Co0.1O2 (NMC811) Cathodes during Electrochemical Cycling. *Chem. Mater.* **2019**, *31*, 2545−2554.

(8) Kasnatscheew, J.; Röser, S.; Börner, M.; Winter, M. Do Increased Ni Contents in LiNixMnyCozO2 (NMC) Electrodes Decrease Structural and Thermal Stability of Li Ion Batteries? A Thorough Look by Consideration of the Li+ Extraction Ratio. *ACS Appl. Energy Mater.* **2019**, *2*, 7733−7737.

(9) Li, W.; Erickson, E. M.; Manthiram, A. High-nickel layered oxide cathodes for lithium-based automotive batteries. *Nat. Energy* **2020**, *5*, 26−34.

(10) Xu, C.; et al. Bulk fatigue induced by surface reconstruction in layered Ni-rich cathodes for Li-ion batteries. *Nat. Mater.* **2021**, *20*, 84−92.

(11) Cabana, J.; Kwon, B. J.; Hu, L. Mechanisms of Degradation and Strategies for the Stabilization of Cathode−Electrolyte Interfaces in Li-Ion Batteries. *Acc. Chem. Res.* **2018**, *51*, 299−308.

(12) Xiao, J.; et al. Assessing cathode−electrolyte interphases in batteries. *Nat. Energy* **2024**, *9*, 1463−1473.

(13) Xu, K. Electrolytes and Interphases in Li-Ion Batteries and Beyond. *Chem. Rev.* **2014**, *114*, 11503−11618.

(14) Nelson, K. J.; et al. Studies of the Effect of High Voltage on the Impedance and Cycling Performance of Li[Ni0.4Mn0.4Co0.2]O2/Graphite Lithium-Ion Pouch Cells. *J. Electrochem. Soc.* **2015**, *162*, A1046.

(15) Dose, W. M.; et al. Electrolyte Reactivity at the Charged Ni-Rich Cathode Interface and Degradation in Li-Ion Batteries. *ACS Appl. Mater. Interfaces* **2022**, *14*, 13206−13222.

(16) Leung, K. First-Principles Examination of Multiple Criteria of Organic Solvent Oxidative Stability in Batteries. *Chem. Mater.* **2023**, *35*, 2518−2530.

(17) Giordano, L.; et al. Chemical Reactivity Descriptor for the Oxide-Electrolyte Interface in Li-Ion Batteries. *J. Phys. Chem. Lett.* **2017**, *8*, 3881−3887.

(18) Solchenbach, S.; Metzger, M.; Egawa, M.; Beyer, H.; Gasteiger, H. A. Quantification of PF5 and POF3 from Side Reactions of LiPF6 in Li-Ion Batteries. *J. Electrochem. Soc.* **2018**, *165*, A3022.

(19) Wiemers-Meyer, S.; Winter, M.; Nowak, S. Mechanistic insights into lithium ion battery electrolyte degradation − a quantitative NMR study. *Phys. Chem. Chem. Phys.* **2016**, *18*, 26595−26601.

(20) Campion, C. L.; Li, W.; Lucht, B. L. Thermal Decomposition of LiPF6-Based Electrolytes for Lithium-Ion Batteries. *J. Electrochem. Soc.* **2005**, *152*, A2327.

(21) Jayawardana, C.; Rodrigo, N.; Parimalam, B.; Lucht, B. L. Role of Electrolyte Oxidation and Difluorophosphoric Acid Generation in Crossover and Capacity Fade in Lithium Ion Batteries. *ACS Energy Lett.* **2021**, *6*, 3788−3792.

(22) Ilic, S.; et al. An unwanted guest in the electrochemical oxidation of high-voltage Li-ion battery electrolytes: the life of highly reactive protons. *Energy Environ. Sci.* **2025**, *18*, 8303−8312.

(23) Aurbach, D.; et al. Review on electrode−electrolyte solution interactions, related to cathode materials for Li-ion batteries. *J. Power Sources* **2007**, *165*, 491−499.

(24) Renfrew, S. E.; McCloskey, B. D. Residual Lithium Carbonate Predominantly Accounts for First Cycle CO2 and CO Outgassing of Li-Stoichiometric and Li-Rich Layered Transition-Metal Oxides. *J. Am. Chem. Soc.* **2017**, *139*, 17853−17860.

(25) Edström, K.; Gustafsson, T.; Thomas, J. O. The cathode−electrolyte interface in the Li-ion battery. *Electrochim. Acta* **2004**, *50*, 397−403.

(26) Gauthier, M.; et al. Electrode−Electrolyte Interface in Li-Ion Batteries: Current Understanding and New Insights. *J. Phys. Chem. Lett.* **2015**, *6*, 4653−4672.

(27) Yu, Y.; et al. Coupled LiPF6 Decomposition and Carbonate Dehydrogenation Enhanced by Highly Covalent Metal Oxides in High-Energy Li-Ion Batteries. *J. Phys. Chem. C* **2018**, *122*, 27368−27382.

(28) Jung, R.; Metzger, M.; Maglia, F.; Stinner, C.; Gasteiger, H. A. Chemical versus Electrochemical Electrolyte Oxidation on NMC111, NMC622, NMC811, LNMO, and Conductive Carbon. *J. Phys. Chem. Lett.* **2017**, *8*, 4820−4825.

(29) Sahore, R.; et al. Revisiting the Mechanism Behind Transition-Metal Dissolution from Delithiated LiNixMnyCozO2 (NMC) Cathodes. *J. Electrochem. Soc.* **2020**, *167*, 020513.

(30) Rynearson, L.; Antolini, C.; Jayawardana, C.; Yeddala, M.; Hayes, D.; Lucht, B. L. Speciation of Transition Metal Dissolution in Electrolyte from Common Cathode Materials. *Angew. Chem., Int. Ed.* **2024**, *63*, No. e202317109.

(31) Song, Y.; et al. The significance of imperceptible crosstalk in high-energy batteries. *Energy Storage Mater.* **2023**, *63*, 103018.

(32) Gowda, S. R.; et al. Oxidation state of cross-over manganese species on the graphite electrode of lithium-ion cells. *Phys. Chem. Chem. Phys.* **2014**, *16*, 6898−6902.

(33) Vissers, D. R.; et al. Role of Manganese Deposition on Graphite in the Capacity Fading of Lithium Ion Batteries. *ACS Appl. Mater. Interfaces* **2016**, *8*, 14244−14251.

(34) Xu, C.; Reeves, P. J.; Jacquet, Q.; Grey, C. P. Phase Behavior during Electrochemical Cycling of Ni-Rich Cathode Materials for Li-Ion Batteries. *Adv. Energy Mater.* **2021**, *11*, 2003404.

(35) Liu, H.; et al. Intergranular Cracking as a Major Cause of Long-Term Capacity Fading of Layered Cathodes. *Nano Lett.* **2017**, *17*, 3452−3457.

(36) Li, J.; Downie, L. E.; Ma, L.; Qiu, W.; Dahn, J. R. Study of the Failure Mechanisms of LiNi0.8Mn0.1Co0.1O2 Cathode Material for Lithium Ion Batteries. *J. Electrochem. Soc.* **2015**, *162*, A1401.

(37) Wandt, J.; Freiberg, A. T. S.; Ogrodnik, A.; Gasteiger, H. A. Singlet oxygen evolution from layered transition metal oxide cathode materials and its implications for lithium-ion batteries. *Mater. Today* **2018**, *21*, 825−833.

(38) Leung, K.; Zhang, M. Hybrid Density Functional Theory Comparison of Oxygen Release and Solvent Decomposition Kinetics on LixNiO2 Surfaces. *J. Phys. Chem. Lett.* **2024**, *15*, 4686−4693.

(39) Jung, R.; Metzger, M.; Maglia, F.; Stinner, C.; Gasteiger, H. A. Oxygen Release and Its Effect on the Cycling Stability of LiNixMnyCozO2 (NMC) Cathode Materials for Li-Ion Batteries. *J. Electrochem. Soc.* **2017**, *164*, A1361.

(40) Ryu, H.-H.; Park, K.-J.; Yoon, C. S.; Sun, Y.-K. Capacity Fading of Ni-Rich Li[NixCoyMn1−x−y]O2 ($0.6 \leq x \leq 0.95$) Cathodes for High-Energy-Density Lithium-Ion Batteries: Bulk or Surface Degradation? *Chem. Mater.* **2018**, *30*, 1155−1163.

(41) Pritzl, D.; Solchenbach, S.; Wetjen, M.; Gasteiger, H. A. Analysis of Vinylene Carbonate (VC) as Additive in Graphite/LiNi0.5Mn1.5O4 Cells. *J. Electrochem. Soc.* **2017**, *164*, A2625.

(42) Michan, A. L.; et al. Fluoroethylene Carbonate and Vinylene Carbonate Reduction: Understanding Lithium-Ion Battery Electrolyte Additives and Solid Electrolyte Interphase Formation. *Chem. Mater.* **2016**, *28*, 8149−8159.

(43) Dai, H.; et al. Exploring the Role of an Electrolyte Additive in Suppressing Surface Reconstruction of a Ni-Rich NMC Cathode at Ultrahigh Voltage via Enhanced In Situ and Operando Characterization Methods. *ACS Appl. Mater. Interfaces* **2024**, *16*, 8639−8654.

(44) Kubot, M.; Balke, L.; Scholz, J.; Wiemers-Meyer, S.; Karst, U.; Hayen, H.; Hur, H.; Winter, M.; Kasnatscheew, J.; Nowak, S. High-Voltage Instability of Vinylene Carbonate (VC): Impact of Formed Poly-VC on Interphases and Toxicity. *Adv. Sci.* **2024**, *11*, 2305282.

(45) Chang, C.-C.; Hsu, S.-H.; Jung, Y.-F.; Yang, C.-H. Vinylene carbonate and vinylene trithiocarbonate as electrolyte additives for lithium ion battery. *J. Power Sources* **2011**, *196*, 9605−9611.

(46) Mosallanejad, B.; et al. Insights into the efficient roles of solid electrolyte interphase derived from vinylene carbonate additive in rechargeable batteries. *J. Electroanal. Chem.* **2022**, *909*, 116126.

(47) Li, Y.; Li, W.; Shimizu, R.; Cheng, D.; Nguyen, H.; Paulsen, J.; Kumakura, S.; Zhang, M.; Meng, Y. S. Elucidating the Effect of Borate Additive in High-Voltage Electrolyte for Li-Rich Layered Oxide Materials. *Adv. Energy Mater.* **2022**, *12*, 2103033.

(48) Wu, F.; Mullaliu, A.; Diemant, T.; Stepien, D.; Parac-Vogt, T. N.; Kim, J.; Bresser, D.; Kim, G.; Passerini, S. Beneficial impact of lithium bis(oxalato)borate as electrolyte additive for high-voltage nickel-rich lithium-battery cathodes. *InfoMat* **2023**, *5*, No. e12462.

(49) Rinkel, B. L. D.; Vivek, J. P.; Garcia-Araez, N.; Grey, C. P. Two electrolyte decomposition pathways at nickel-rich cathode surfaces in lithium-ion batteries. *Energy Environ. Sci.* **2022**, *15*, 3416−3438.

(50) Self, J.; Aiken, C. P.; Petibon, R.; Dahn, J. R. Survey of Gas Expansion in Li-Ion NMC Pouch Cells. *J. Electrochem. Soc.* **2015**, *162*, A796−A802.

(51) Von Cresce, A.; Xu, K. Preferential Solvation of Li+ Directs Formation of Interphase on Graphitic Anode. *Electrochem. Solid-State Lett.* **2011**, *14*, A154.

(52) Trevisanello, E.; Ruess, R.; Conforto, G.; Richter, F. H.; Janek, J. Polycrystalline and Single Crystalline NCM Cathode Materials—Quantifying Particle Cracking, Active Surface Area, and Lithium Diffusion. *Adv. Energy Mater.* **2021**, *11*, 2003400.

(53) Zhou, J.; Wang, X.; Sun, Z.; Gu, C.; Gao, J. The mechanisms of ·OH formation in MnO2 and oxalate system: Implication for ATZ removal. *J. Hazard. Mater.* **2024**, *470*, 134213.

(54) Xu, M.; et al. Investigation and application of lithium difluoro(oxalate)borate (LiDFOB) as additive to improve the thermal

stability of electrolyte for lithium-ion batteries. *J. Power Sources* **2011**, *196*, 6794−6801.